

New insights into the electrochemical reduction of carbon dioxide on metallic copper surfaces†

Kendra P. Kuhl,^a Etosha R. Cave,^b David N. Abram^c and Thomas F. Jaramillo^{*c}

Received 30th January 2012, Accepted 23rd February 2012

DOI: 10.1039/c2ee21234j

We report new insights into the electrochemical reduction of CO₂ on a metallic copper surface, enabled by the development of an experimental methodology with unprecedented sensitivity for the identification and quantification of CO₂ electroreduction products. This involves a custom electrochemical cell designed to maximize product concentrations coupled to gas chromatography and nuclear magnetic resonance for the identification and quantification of gas and liquid products, respectively. We studied copper across a range of potentials and observed a total of 16 different CO₂ reduction products, five of which are reported here for the first time, thus providing the most complete view of the reaction chemistry reported to date. Taking into account the chemical identities of the wide range of C₁–C₃ products generated and the potential-dependence of their turnover frequencies, mechanistic information is deduced. We discuss a scheme for the formation of multicarbon products involving enol-like surface intermediates as a possible pathway, accounting for the observed selectivity for eleven distinct C₂+ oxygenated products including aldehydes, ketones, alcohols, and carboxylic acids.

Introduction

The development of a cost effective process for the electrochemical reduction of CO₂ could enable a shift to a sustainable energy economy and chemical industry.^{1–3} Coupled to a renew-

able energy source such as wind or solar, such a process could generate carbon neutral fuels or industrial chemicals that are conventionally derived from petroleum. A key technological challenge necessary to enable such a process is the development of catalysts that are active and selective for this reaction, *i.e.* catalysts that can reduce CO₂ at low overpotentials, generate desirable products at high current densities over long periods of time, and do so selectively without the formation of unwanted byproducts. Unfortunately, of the many electrocatalyst materials previously investigated, none are both efficient and selective,^{4–12} and the most common products of CO₂ reduction are CO and formate, which are not as readily used as fuels as are hydrocarbons or alcohols. Copper metal is the only known material capable of catalyzing the formation of significant amounts of

^aDepartment of Chemistry, Stanford University, Stanford, CA, 94305-5025, USA

^bDepartment of Mechanical Engineering, Stanford University, Stanford, CA, 94305-5025, USA

^cDepartment of Chemical Engineering, Stanford University, Stanford, CA, 94305-5025, USA. E-mail: jaramillo@stanford.edu; Fax: +1 725 7294; Tel: +1 498 6879

† Electronic supplementary information (ESI) available. See DOI: 10.1039/c2ee21234j

Broader context

For intermittent renewable sources such as wind and solar to compete with fossil fuels, technologies must be developed that can store and time-shift the energy to match demand. Hence, there is significant interest in the electrochemical conversion of CO₂ into a hydrocarbon fuel; coupling such a process to renewable electricity could generate carbon-neutral fuels for use in stationary power or in the transportation sector. The conversion of CO₂ to other organic products is also of significant value as CO₂ could in principle replace fossil fuels as a feedstock in the chemical industry, enabling a pathway for sustainable chemicals. Research over the past several decades has shown that copper metal is unique among catalysts explored so far for its ability to convert CO₂ to the hydrocarbons methane and ethylene with a high current efficiency. A high overpotential is required, however, and the reaction does not proceed with high selectivity, problems that are faced by other catalysts for CO₂ reduction as well. Further study into CO₂ reduction on copper will lead to a deeper understanding of the reaction chemistry and can eventually lead to the design of more efficient and selective catalysts.

hydrocarbons at high reaction rates over sustained periods of time; however, an overpotential of almost 1 V is required and a fairly broad mix of major and minor products are produced, including hydrogen, ethylene, and methane.¹³ Although copper is not an ideal catalyst for CO₂ reduction, understanding its unique ability to catalyze hydrocarbon formation would aid in the design of new catalysts that are active at a lower overpotential and with better product control.

A number of excellent reviews^{14–16} summarize the literature associated with CO₂ reduction on copper. The mechanism of the reaction is not clearly understood, but CO appears to be an important intermediate. Electroreduction of CO leads to a similar product distribution as observed for CO₂ reduction,¹⁷ producing both ethylene and methane. The data suggests that different rate determining steps lead to the production of ethylene and methane from CO. Ethylene formation is favored over methane at lower overpotentials and different Tafel slopes and transfer coefficients have been calculated for each product.¹⁴ It is unknown whether CO or a more reduced C₁ species is coupled to make C₂ and longer carbon chain products. Recent work to shed light on the CO₂ reduction mechanism includes the use of density functional theory (DFT) to predict intermediates involved in the formation of methane^{18,19} and from an experimental standpoint, the use of on-line mass spectrometry to identify the products formed from the electroreduction of various compounds that could be intermediates on the ethylene pathway.²⁰

In this study on copper catalyzed electroreduction, we report on an experimental methodology that allows for product identification and quantification with unprecedented sensitivity. This involved the design and fabrication of a custom electrochemical reactor with a large working electrode and small electrolyte volume, coupled to two different forms of product analysis by means of gas chromatography (GC) and nuclear magnetic resonance (NMR) spectroscopy. With this system, we measured CO₂ reduction products over a range of potentials on a copper metal foil. The major products observed are in good agreement with past studies; however, three new important observations were found in our study that provide key insight into the surface chemistry and mechanistic aspects of CO₂ reduction on copper: (1) We detected a total of 16 different reaction products – significantly more than any previous study – a number of which were novel products that were for the first time identified and quantified from a copper surface. Of the 16 reaction products detected, 12 of them were C₂ or C₃ species, comprised of a broad mix of oxygenated species including hydrocarbons, ketones, aldehydes, carboxylic acids, and alcohols. (2) Regarding this broad range of different C₂ and C₃ species detected, we found that the partial current density and therefore the turnover frequency (TOF) of these products generally track that of ethylene across the range of potentials investigated. (3) We recognized that all of the C₂ and C₃ products detected – without exception – could have plausibly been produced *via* the dehydroxylation of an earlier, less reduced product in its enol or diol form. These observations lead us to a hypothesis that the chemistry to generate the wide range of C₂ and C₃ products could occur through an enol-like surface intermediate; the appearance of the many multicarbon oxygenate products can be conveniently explained in this way and might potentially be used as

a guide to determining the C₁ and C₂ species involved in C–C bond formation.

Methods

Surface preparation

Copper foil (thickness 1.0 mm, Aldrich, 99.999% metals basis) was used as the working electrode. The surface preparation prior to each experiment consisted of mechanically polishing (400G sandpaper, 3M) until no discoloration was visible and then electropolishing in phosphoric acid (85% in H₂O, Aldrich, 99.99% metals basis) potentiostatically at 2.1 V vs. a graphite foil (0.13 mm thick, Alfa Aesar, 99.8% metals basis) counter electrode placed at a distance of 1.5 cm. X-ray photoelectron spectroscopy (XPS, PHI Versaprobe) and scanning electron microscopy (SEM, FEI XL30 Sirion) were used to characterize the surface.

Electrochemical cell

A custom electrochemical cell made from polycarbonate and fitted with Teflon coated silicon o-rings (McMaster-Carr) was employed for CO₂ electrolysis experiments (Fig. 1). The cell maintained the working electrode parallel to the counter electrode to achieve a uniform voltage. An anion exchange membrane (Selemion AMV, AGC Inc.) was used to separate the working and counter electrode compartments to prevent the oxidation of reduced CO₂ products, although the membrane did not prohibit passage of the anionic products acetate and formate, which were detected on the counter electrode side of the cell in low concentration after electrolysis. The cell was designed to have a large electrode area (1.5 cm × 3 cm) and a small electrolyte volume (8 mL) in each of the two compartments, along with a gas headspace of approximately 3 mL above the electrolyte on each side of the membrane. CO₂ (5.0, Praxair), regulated by a mass flow controller (π MFC, MKS Instruments) at 20 sccm, flowed through the cell during electrolysis. CO₂ flow through the

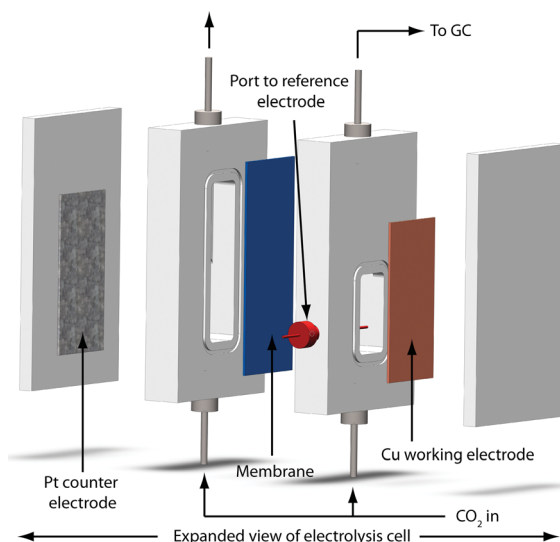


Fig. 1 Schematic of the electrochemical cell and experimental setup used in electrolysis experiments.

cell was needed to see large current efficiencies for CO₂ reduction products, presumably because of mass transport limitations in a quiescent cell. The flow rate of 20 sccm was chosen to ensure sufficient CO₂ transport to the surface while preventing interference from gas bubbles striking the surface. The CO₂ was humidified with water by passing it through a bubbler before it entered the electrolysis cell in order to minimize the evaporation of volatile liquid phase products. For each electrolysis experiment the cell was assembled with copper as the working electrode and platinum as the counter electrode. An Ag/AgCl electrode (Accumet) was used as the reference. The distance between the working and reference electrodes was kept small (0.5 cm) to reduce solution resistance. A 0.1 M solution of KHCO₃ (Sigma-Aldrich, 99.99% metals basis) was prepared with 18.2 MΩ deionized water from a Millipore system and used as the electrolyte. The pH of the electrolyte purged with CO₂ was 6.8.

Electrolysis

Electrochemistry was carried out with an electrochemical impedance spectroscopy (EIS) capable channel in a Biologic VSP or VMP3 potentiostat. All electrochemical data was collected *vs.* a Ag/AgCl reference and converted to a reversible hydrogen electrode (RHE) scale by $V_{\text{vs. RHE}} = V_{\text{measured vs. Ag/AgCl}} + 0.197 + 0.059 \times \text{pH (of soln)}$ (see ref. 14 for a discussion of overpotential for CO₂ reduction). Potentiostatic EIS (Figure S1) showed that 10 kHz was an appropriate frequency to determine the uncompensated solution resistance (R_u). The potentiostat compensated for 85% of the value of R_u and the last 15% was post-corrected to arrive at accurate potentials (see Supporting Information for details). EC-Lab software was used to link different techniques without returning to open circuit for each electrolysis experiment. At the beginning of each experiment, the value of R_u was determined prior to taking an initial cyclic voltammogram (CV). After completion of the CV, the value of R_u was determined again in case it had changed due to the reduction of the native CuO_x layer. Then, the electrolysis potential was applied for 1 h (chronoamperometry). During this time, the electrolysis was interrupted briefly to update the value of R_u compensated for by the potentiostat (see Figure S2 for a description of changes in R_u during electrolysis). After the completion of the chronoamperometry, a CV was again taken to test for changes in electrode activity. For experiments run at less negative voltages, the CVs were taken out to −1.05 V *vs.* RHE to be sure that any CuO_x on the surface was reduced before holding potentiostatically at the electrolysis voltage.

Product quantification

One mL aliquots of the reactor exhaust were injected *via* an automated sample loop into a gas chromatograph (GC, SRI 8610C in the Multi-Gas #3 configuration). Aliquots were collected after 5 mins, 23 mins, 41 mins, and 59 mins of chronoamperometry to determine the concentration of gaseous products, which included hydrogen, methane, CO, and ethylene (Figure S3). The current efficiency was calculated by determining the number of coulombs needed to produce the measured amount of each product then dividing by the total charge passed during the time of the GC sampling. The steady state current

efficiency reported at a given potential is the average of the current efficiencies measured at 23, 41, and 59 mins. Each potential was repeated three times, in the same fashion, and the average of the three experiments is given in Fig. 5.

Liquid phase products were quantified using 1D ¹H NMR (600 MHz, Varian Inova). Standard curves were made using purchased chemicals over the concentration range of interest, with the internal standards DMSO and phenol, in 0.1 M KHCO₃. The water peak was suppressed by a presaturation sequence. NMR parameters used (see Supporting Information Figure S4) were identical between collected spectra to make standard curves and in the subsequent quantification of products in the electrolyte. 700 μL of the electrolyte containing CO₂ reduction products after the hour long electrolysis was mixed with 35 μL of a 10 mM dimethyl sulfoxide (DMSO) and 50 mM phenol for use as internal standards in D₂O for NMR analysis (Figure S4). The ratio of the area of the formate peak to the area of the phenol peak and the ratio of the other products' peak areas to the DMSO peak area were compared to standard curves (Figure S5) to quantify the concentrations of the reaction products. The coulombs needed to produce that concentration of each product was calculated and divided by the total coulombs passed during the chronoamperometry to determine the current efficiency. ¹H NMR allowed for quantification of all of the liquid phase products identified in this study, with the exception of glyoxal as its signal was obscured by the water peak and thus required the use of ¹³C NMR for detection.

Product identification

To determine and confirm the identities of the liquid phase CO₂ reduction products described in this work, more advanced NMR experiments were performed. A 2D homonuclear correlation spectroscopy (COSY) experiment was employed (800 MHz, Agilent VNMRs) to determine which proton peaks were correlated in the ¹H NMR spectra. ¹³CO₂ (99% enriched in ¹³C, Isotec) was reduced using the above electrolysis procedure and the resulting ¹³C labeled products were subjected to 1D ¹³C (500 MHz, Varian Inova) and 2D (¹H/¹³C) heteronuclear single-quantum coherence (HSQC) (800 MHz, Varian Inova) NMR experiments. ¹³C NMR showed the carbon peaks of products and the 2D HSQC experiment correlated peaks observed in ¹H spectra to peaks in the ¹³C spectra. 1D ¹H (600 MHz, Varian Inova) and 1D ¹³C (500 MHz, Varian Inova) spectra of an authentic sample of each product were matched to the observed CO₂ reduction product peaks to verify their identity (Table S1).

Results and discussion

Surface preparation

It is important to ensure that the system is free of contaminants so that electrochemical and product measurements can truly be attributed to the activity of copper.²¹ SEM images of the copper electrode surface are shown after mechanical polishing (Fig. 2A) and subsequent electropolishing (Fig. 2B), resulting in a smoother surface free of impurities. Electropolishing was performed in the copper ion diffusion limited regime of the CV (Fig. 2C) before oxygen evolution begins and before surface roughening can occur.²² Fig. 2D shows XPS measurements taken

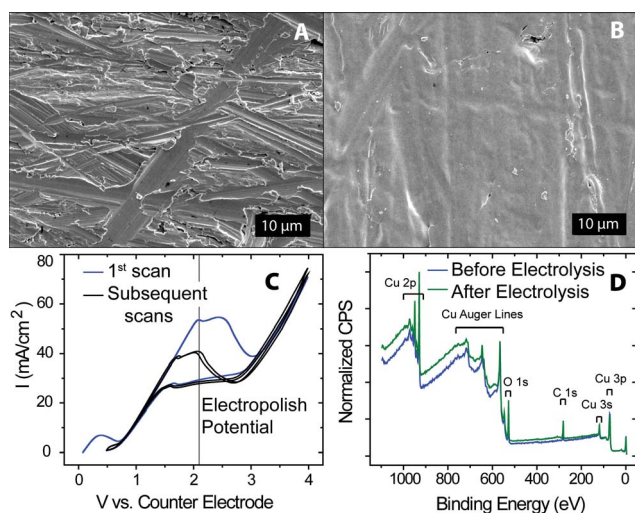


Fig. 2 Surface preparation of the Cu working electrode. A) SEM of the sandpapered surface. B) SEM of the surface after electropolishing. C) Two electrode CV taken of the Cu electrode in 85% phosphoric acid indicating the potential where electropolishing occurred. D) XPS of the surface before and after an electrolysis experiment.

before and after electrolysis. The peaks are attributable to only Cu, O, and C,^{23,24} revealing that no metal impurities are present within the detection limits of XPS. The O likely arises from a thin native oxide at the copper surface as well as from adventitious organics which are also responsible for the C signal.

Electrolysis setup

There exists no standard experimental methodology for studying CO₂ electroreduction. In order to obtain the most meaningful data, an experimental setup must provide accurate electrochemical measurement of the current and voltage while also allowing for product identification and quantification with high sensitivity for all possible products (any organic compound consisting of C, H, and/or O). To generate detectable amounts of products, relatively large currents are necessary. Thus, in this study, we investigated current densities in the range of negative 0.5–20 mA cm⁻² over the course of an hour. Not coincidentally, this current density range is relevant for solar fuel synthesis as 10 mA cm⁻² of CO₂ reduction current matches the solar photon flux for a ~ 10% efficient device under AM1.5G sunlight (see Supporting Information for details).

An important consequence of this relatively large magnitude of current is that it can lead to substantial errors in the measurement of voltage due to iR-drop in the electrochemical cell, unless one adequately compensates for R_u.²⁵ For instance, in our experimental setup we typically measure a value of 16 Ω for R_u, and with a total current of 45 mA (10 mA cm⁻²) this leads to a 0.72 V difference between the potentiostat reading and the true voltage at the working electrode if iR compensation is not used. This discrepancy between actual and applied voltage requires the use of iR compensation in order to get reproducible data that is comparable between different laboratories and experimental setups.

The electrochemical cell employed was designed to have a large electrode surface area to electrolyte volume ratio to

maximize the concentration of liquid phase products in the electrolyte. The higher product concentrations using our custom electrochemical cell compared to a traditional H-type electrolysis cell^{7,26} allowed for the detection of several minor products that have not previously been reported probably due to (1) their low concentration, and (2) the methods of detection used in previous studies. A principal advantage of the experimental methodology reported in this work was the use of NMR to measure liquid phase products. NMR required no purification or separation of the products, thus allowing for analysis with a lower likelihood for product loss to occur. In addition to quantitative information, considerable structural information was also present in the NMR spectra, allowing for more certain product assignment when compared to traditional chromatography where retention time alone is used for identification. As will be seen below, the development of an experimental methodology to identify and quantify all possible products, major and minor, can help substantially in deducing reaction mechanisms.

CO₂ reduction products

Table 1 shows the sixteen products of CO₂ reduction on a copper electrode identified in this work along with structure, number of electrons, and reduction potential at pH 6.8 vs. RHE calculated from tabulated thermodynamic data.^{27,28} Nine of these sixteen products have been commonly reported in previous studies: methane, ethylene, CO, formate, ethanol, n-propanol, allyl

Table 1 Products of CO₂ reduction along with the number of electrons needed to produce each one and its standard reduction potential at pH 6.8. Products shown in green appear in only a few past studies, and products shown in blue are reported here for the first time

Product	# e ⁻	E	Product	# e ⁻	E
Formate 	2	-0.02	Acetaldehyde 	10	0.05
Carbon monoxide 	2	-0.10	Ethanol 	12	0.09
Methanol 	6	0.03	Ethylene 	12	0.08
Glyoxal 	6	-0.16	Hydroxyacetone 	14	0.46
Methane 	8	0.17	Acetone 	16	-0.14
Acetate 	8	-0.26	Allyl alcohol 	16	0.11
Glycolaldehyde 	8	-0.03	Propionaldehyde 	16	0.14
Ethylene glycol 	10	0.20	1-Propanol 	18	0.21

alcohol, acetaldehyde, and propionaldehyde.⁴ Acetate²⁹ and methanol³⁰ are two species that have been identified as products previously; however they have appeared in only a few reports.

Methanol has been reported as a product of electrochemical reduction on a Cu₂O surface, but has not been reported previously as a product on metallic Cu surfaces. To verify that the methanol was not produced only at the beginning of the reaction before the native CuO_x surface had been reduced, aliquots of the electrolyte were examined for methanol after 5 min and 1 h. The amount of methanol present after 1 h was significantly greater than the amount present after 5 min, which indicates that methanol was produced throughout the electrolysis, not solely at the beginning. The production rate of methanol is roughly 4 orders of magnitude less than that of methane, which is consistent with predictions made based on DFT calculated thermodynamics.³¹

The five remaining products in the table, ethylene glycol, glycolaldehyde, hydroxyacetone, acetone, and glyoxal, are oxygenated C₂ and C₃ products that have never been reported before to the best of our knowledge. Glyoxal and hydroxyacetone are particularly intriguing. They are the C₂ and C₃ products requiring the fewest number of electron and proton transfers to form. This demonstrates that at least some C–C coupling occurs between C₁ species at this early stage of reduction. The other novel products reported here are also less reduced than previously reported products, perhaps shedding light on intermediate species present on the pathway to ethylene and propanol, the most reduced C₂ and C₃ products detected.

With our experimental methodology, the detection limit for methane, ethylene, CO, and formate is approximately 10 μA cm⁻² for each product. The detection limit for ethanol, acetaldehyde, acetate, methanol, ethylene glycol, glycolaldehyde, hydroxyacetone, and acetone is approximately 50 μA cm⁻². The approximate detection limit for n-propanol and propionaldehyde is 100 μA cm⁻² while for allyl alcohol and glyoxal it is 400 μA cm⁻². The detection limits for these latter two compounds are higher because the peak used for quantification of allyl alcohol is coupled to multiple protons, and glyoxal can only be observed using ¹³C NMR, which is less sensitive and thus not quantified in this study. Formation of a product in quantities below its detection limit cannot be ruled out; however, for most species our methodology achieves detection limits in the range of 10–100 μA cm⁻², which is quite sensitive, particularly for liquid-phase products.

A significant fraction of the observed CO₂ reduction products are oxygenates. The presence of hydroxyl and/or carbonyl moieties in many of the C₂ and C₃ products suggests that the C–C coupling step occurs before at least one of the two carbon-oxygen bonds in CO₂ is broken. This is different from a Fischer–Tropsch type mechanism previously suggested, in which methylene groups on the surface are responsible for chain growth.²⁶ Many of the detected products contain carbonyls, compounds which possess enol tautomers and can undergo hydration in aqueous solution to become diols (Fig. 3). These complex equilibria in an aqueous environment make it difficult to ascertain whether a detected product was released from the electrode surface in that form or whether a different species was released from the electrode and equilibrated to a more stable form once in solution. Fig. 3 shows all the carbonyl containing products in their diol,

Product Name	Diol $\xrightleftharpoons[+H_2O]{-H_2O}$	Keto \rightleftharpoons	Enol
Glyoxal		 	
Glycolaldehyde			
Acetate			
Acetaldehyde			
Hydroxyacetone			
Propionaldehyde			
Acetone			

Fig. 3 Equilibria of carbonyl containing products in water. Blue indicates the most stable structure under our experimental conditions.

keto, and enol forms. The most thermodynamically favored form, the one detected by NMR in solution, is indicated in blue and is in agreement with known aldehyde hydration equilibria.^{32–34} We note that the enol tautomer is generally thermodynamically unfavorable in aqueous solution; for example, the difference in $\Delta G_f^\circ(\text{aq})$ of keto vs. enol form of acetaldehyde is $-8.54 \text{ kcal mol}^{-1}$.³⁵ Thus one would expect a compound desorbing from the electrode in its enol form to quickly convert to its diol and/or keto form.³⁶

It is also important to determine whether or not detected organic species could arise from sources other than CO₂ reduction.⁴ To examine this possibility, we conducted a control experiment in which the electrolyte was left overnight in the polycarbonate electrolysis cell with CO₂ flowing and no applied potential. No products were detected. The reaction was also run in a cell made of Kel-F® and the same products were observed as those measured from electrolysis in the polycarbonate cell. Thus, we can confirm that these products do in fact result from the CO₂ electroreduction process and not from a contamination source in the cell.

Recently, it has been pointed out that aldehydes can decompose spontaneously and that their decomposition products can be erroneously assigned as products of the reaction.³⁷ To be sure the observed products were stable under electrolysis and storage conditions, an individual solution of each of the carbonyl products was prepared, placed in the electrolysis setup with CO₂ flowing for 1.5 h, and then examined by NMR; no decomposition was observed.

Measured current vs. potential

Fig. 4A shows the current vs. time profile of a representative electrolysis experiment at each voltage. The current remains stable over the course of the hour at most potentials, indicating little deactivation of the copper electrode due to impurities or otherwise. At -1.18 V vs. RHE, the most negative potential studied, there is a small but noticeable decline in the absolute value of the current over time. The change in current could potentially arise from slight increases in the temperature of the cell at the highest current densities (see Supporting Information), resulting in a modest decrease in the solubility of CO_2 . At the higher current densities, the data becomes somewhat noisy as bubbles begin to form on the electrode surface, which cover areas of the electrode until they grow large enough to be released, causing fluctuations in the current. iR-compensation may also contribute to the changes in current as the bubbles make it more difficult for the potentiostat to maintain a constant voltage.

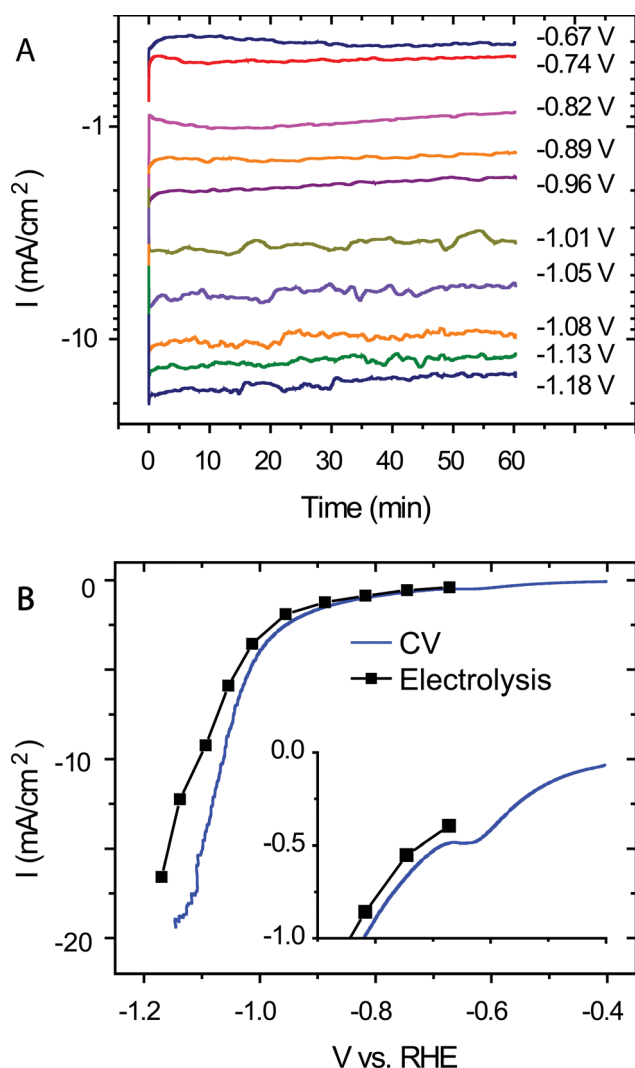


Fig. 4 CO_2 reduction current A) as a function of time at different voltages and B) averaged for all experiments at each voltage and compared to a CV taken at 50 mV s^{-1} .

Fig. 4B shows the average current for each voltage overlaid with a CV taken before an electrolysis experiment. The current observed during electrolysis matches that of the CV very well, with the slight decrease in current during electrolysis being attributable to bubble formation. The CV shows a prepeak at -0.63 V vs. RHE that has previously been attributed to the onset of CO_2 reduction.¹⁶ The reduction of a CuO_x surface species has also been suggested to give rise to this feature.³⁸ The electrolysis voltages studied herein were all cathodic of this prepeak feature.

Products vs. potential

Fig. 5, which plots the current efficiency of each product as a function of potential, is divided into three panels in which major, intermediate, and minor products are grouped. The data is consistent with previously reported data for copper electrodes; however, the data extends to a higher overpotential than previous reports and several new products are reported that have not been detected before.^{16,39} At low overpotentials (before reaching -0.75 V vs. RHE), only hydrogen, CO, and formate are observed. As the overpotential increases, the percentage of the current going to hydrogen

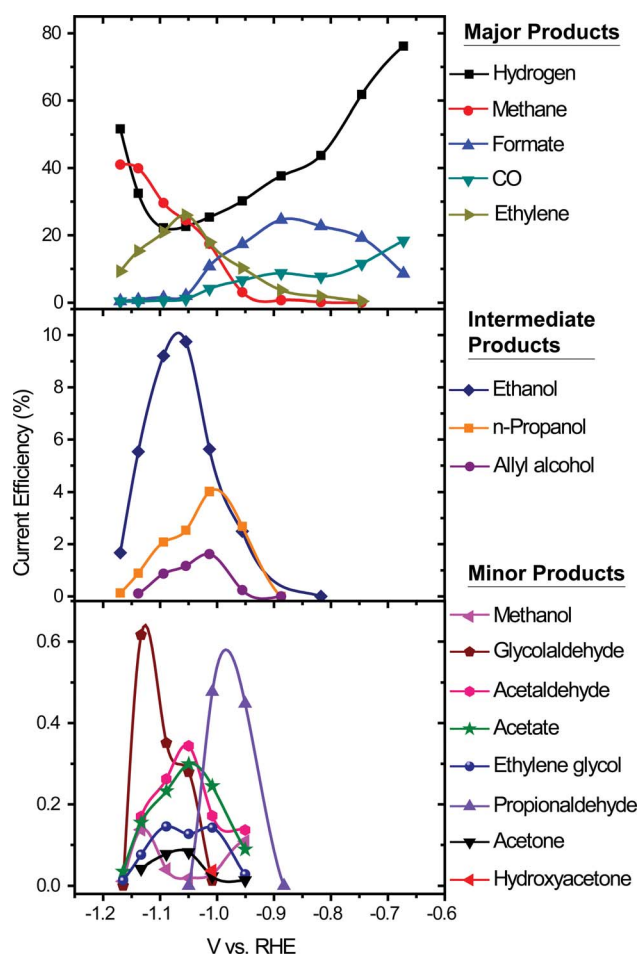


Fig. 5 Current efficiency for each product as a function of potential is shown for major, intermediate range, and minor products.

evolution decreases while the percent going to CO₂ reduction products increases. At -0.75 V vs. RHE, ethylene and methane are the first hydrocarbons to be observed, with ethylene favoured over methane. The current efficiencies for methane and ethylene rise steadily for the next ~ 200 mV, and at -0.96 V vs. RHE, drastic changes in reaction selectivity are observed. First and most importantly, a significant number of new C₁–C₃ products begin to emerge. Secondly, the selectivities towards CO and formate begin to decrease slightly. The current efficiencies for all C₂ and C₃ products continue to increase with increasing overpotential, until a peak is reached around -1.05 V (± 0.1 V) vs. RHE. At this potential, the current efficiencies for CO and formate have declined to values close to zero. The current efficiency for H₂ has also been decreasing up to this point, but at -1.05 V vs. RHE, the selectivity for H₂ reverses course and now increases with increasing overpotential. At very high overpotentials, beyond -1.05 V vs. RHE, selectivities towards all C₁–C₃ products are in decline with the sole exception of methane, whose current efficiency continues to rise along with that of H₂. Previous reports have not shown current efficiencies at such negative potentials where methane formation is favored so definitively over other CO₂ products, concomitant with increased hydrogen evolution. At the most negative potential investigated in this study, -1.18 V vs. RHE, methane and H₂ account for over 90% of the current efficiency.

Current efficiency is an important metric by which to understand CO₂ reduction selectivity; however, one must bear in mind that in these plots (Fig. 5) the total current density is changing significantly across the potential window. Multiplying the total current density at a given potential by the current efficiency for each product allows one to construct a plot of the partial current density going toward the formation of each product vs. potential, shown in Fig. 6. To facilitate the discussion of mechanistic implications, Fig. 6 is grouped differently than in Fig. 5, with three panels showing H₂ & C₁ products, C₂ products, and C₃ products, respectively. As the partial current density for a given product is proportional to its TOF (see Figure S7 in the Supplementary Information) analyzing reaction rates by means of partial current density can provide a clearer basis by which to understand reaction kinetics.

For example, as described earlier, in the range of -0.7 to -1.0 V the current efficiency plot (Fig. 5) shows a significant decrease in H₂. However, the partial current density (Fig. 6) and TOF plots (Figure S7) show that the rate of H₂ formation stays fairly constant in this potential region, and in fact actually increases slightly (by a factor of 2). Thus, the decrease in selectivity is not due to a decrease in H₂ TOF, but rather due to more rapidly increasing TOFs for other products.

In this same potential region, the partial current densities and TOFs for CO and formate are fairly constant. While this is consistent with previous reports, it is unclear why the TOFs for these products lack a strong potential dependence. Beyond -1.0 V, there is a slight decrease in current producing CO and formate and an increase in current going to H₂. CO₂ reduction products requiring more than 2 electrons increase in partial current until they reach approximately -1.08 V. After this potential, the current going to all C₂ and C₃ products decreases sharply, but the current to methane continues to rise within the voltage range measured.

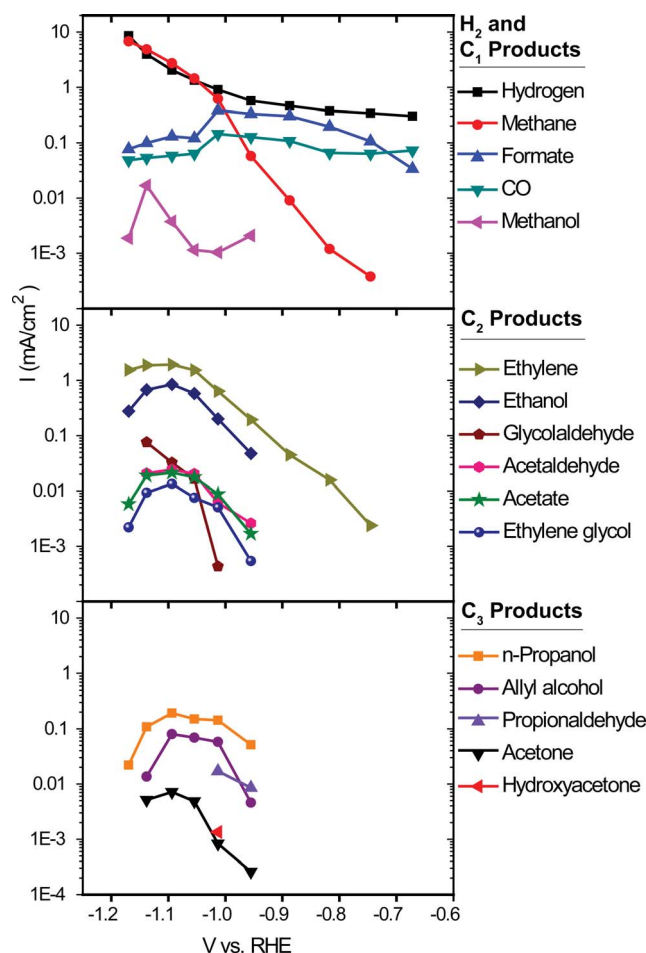


Fig. 6 Tafel plot of the partial current going to each product.

One possible explanation for the difference in the slopes of methane and ethylene as well as for their different behaviors at high overpotential is that there are different rate determining steps leading to each of these products, as suggested in previous studies.¹⁴ Coverage effects could also play a significant role in the measured TOF, as the coverage of certain surface adsorbates are likely to change with applied electrochemical potential, as will be discussed below. While ethylene and methane exhibit different behavior as a function of applied potential, Fig. 6 has another important feature: the partial current densities of all C₂ and C₃ products track that of ethylene. This is a critical feature with strong mechanistic implications that will be discussed in further detail below.

Of the multicarbon products, ethylene appears the earliest and has the highest current density. Other C₂ and C₃ products are first detectable at -0.95 V vs. RHE, although it is conceivable that they are present but below the detection limit at less negative potentials. As the overpotential increases, the current going to C₂ and C₃ products first rises and then falls. Note that in Fig. 6, the absence of a data point for a particular product at a given potential indicates that the species was not observed. We also note that the error in the measurement in some of the minor products (e.g. methanol) can be relatively large due to their low concentration in solution (see Supporting Information Table S2), thus for these cases clear trends are not observed.

A mechanistic view of CO₂ reduction on Cu

From our study, it is clear that Cu catalyzes the formation of a large number of CO₂ reduction products, more products than have ever been reported before. Having identified the wide range of products, as well as their partial current densities (*i.e.* TOFs) as a function of applied potential, one can begin to consider the mechanism of CO₂ reduction on a Cu electrode. Any proposed mechanism must account for the formation of all 16 different CO₂ reduction products detected in this study. Of these 16 products, the two with the largest current efficiencies are the hydrocarbons methane and ethylene, while the remaining 14 products are oxygenates, 11 of which are C₂ and C₃ products.

The CO₂ reduction products observed at the lowest overpotential, formate and CO, only require a two electron reduction. It is only at higher overpotential that more reduced products are formed. This is consistent with the pervading view that CO and formate have the lowest kinetic barriers to formation. Further reduction of intermediate CO to hydrocarbons is kinetically more difficult, thus the more reduced products appear only at higher overpotentials.^{17,18}

As mentioned earlier, the fact that all C₂ and C₃ products behave similarly as a function of potential is an important clue in deducing mechanistic information. For C–C coupling to occur, favorable reaction energetics are required as well as sufficient surface coverage of the species involved in the coupling reaction. Irrespective of whether the C–C coupling step is a thermochemical step or an electrochemical step, the electrochemical potential can have a significant impact on the rate of C–C coupling. Two C-containing adsorbates must be adjacent to one another for this to occur, and as the electrochemical potential determines which species are present on the surface as well as their coverage, a potential-dependent C–C coupling rate is expected.

It is not surprising that the C–C coupling rate initially increases with increasing overpotential. The subsequent decrease in C–C coupling with further increasing overpotential, however, can be explained by the proton and electron transfers becoming more favorable at negative potentials. At very negative potentials, surface-bound C₁ species (*e.g.* CO, HCO, *etc.*) are more likely to be reduced all the way to methane and desorb rather than remain as a surface-bound C₁ intermediate involved in coupling. Therefore, at more negative potentials, the TOF for methane increases while C–C coupling decrease due to the lower statistical probability of the appropriate C₁ intermediates encountering one another, a necessary (but insufficient) condition for C–C bond formation to occur. The same principle applies to C₁ and C₂ intermediates coupling to form a C₃ species.

This view of the surface chemistry for CO₂ reduction can explain why at moderate overpotentials, TOFs for C₁–C₃ products all rise together yet at higher overpotentials, only the TOF for methane continues to rise while the TOFs for all other C₁–C₃ species are in decline. The rise in TOF for H₂ at the more negative potentials is also consistent with an increasing TOF for methane, as proton and electron transfers are heavily favored at such negative potentials. This suggests that either the coverage of adsorbed H is increasing at those potentials or that the Heyrovsky mechanism for H–H bond formation – an electrochemical step – becomes the more dominant pathway for hydrogen evolution.^{40,41}

Thus far, we have been able to mechanistically address the major trends in TOF observed in Fig. 6 for all C₁, C₂, and C₃ products, particularly their rise and/or fall as a function of applied potential. Another major mechanistic question involves the wide range of oxygenated products observed, particularly the eleven C₂ and C₃ species including aldehydes, ketones, carboxylic acids, and alcohols. It is an open question as to how Cu produces such a wide variety of oxygenates; the reaction mechanism must account for these diverse products. Ethylene is the only C₂₊ hydrocarbon observed, and given the previously mentioned similarities in TOF trends among all C₂–C₃ products, it is plausible that a pathway to ethylene could be common to the C₂₊ oxygenates as well. If this is indeed the case, it would suggest that at least one of the two C–O bond breaking steps does not occur until fairly late on the pathway from CO₂ to ethylene, otherwise one would expect fewer oxygenated products among C₂ and C₃ species. Note that this does not discount the possibility of multiple pathways to ethylene existing in parallel.

There are many possible explanations for the wide range of C₂ and C₃ oxygenates observed. One possibility is that there are a wide variety of different sites on the Cu surface, with each site geared to produce a different product. This is not unreasonable; a surface with more under-coordinated Cu atoms present has been shown to change the product distribution of CO₂ reduction.⁴² Another hypothesis is that the same type of surface site can catalyze the formation of a number of different C₁ oxygenates which are thermodynamically accessible at high overpotential, and that these diverse C₁ species can couple to form all of the observed products. If the C–C coupling step between the many possible C₁ intermediates are kinetically accessible, this could certainly explain the wide of C₂₊ products observed. Based on our experimental findings, we also consider a third and novel hypothesis: a simple reaction scheme described below in which the same electrochemical step, a dehydroxylation of surface intermediates involving 2 H⁺ and 2 e[−], is repeated over and over to ultimately produce a wide range of oxygenated products of varying degrees of reduction (Fig. 7). As the free energy pathway for dehydroxylation, which would occur after the rate determining step, is unlikely to differ significantly for various C₂ and C₃ surface intermediates, one can expect the trends in production rates for the various species to follow one another as a function of applied potential. This scheme accounts for all of our experimental measurements, and is based on the fact that many of these multicarbon products possess carbonyl groups with enol tautomers and undergo hydration in the electrolyte.

Fig. 7 shows one plausible reaction pathway which can account for the production of all C₂ and C₃ species observed in this study, bearing in mind the carbonyl equilibria addressed in Fig. 3. In this pathway, enol-like intermediates are a major conduit by which C₂ and C₃ products are produced. Intermediates formed on the electrode surface are indicated by orange circles and are drawn in their enol and/or diol form. Blue circles indicate species present in the electrolyte solution as identified by NMR. The pH and protonation state of surface intermediates are unknown, but for simplicity all species are drawn fully protonated. In this scheme, each electrochemical step comes in the form of 2 H⁺ and 2 e[−] transfers, leading to a more reduced product by the replacement of a hydroxyl group (which goes on to form water) by a hydrogen atom. Note that while it is unclear

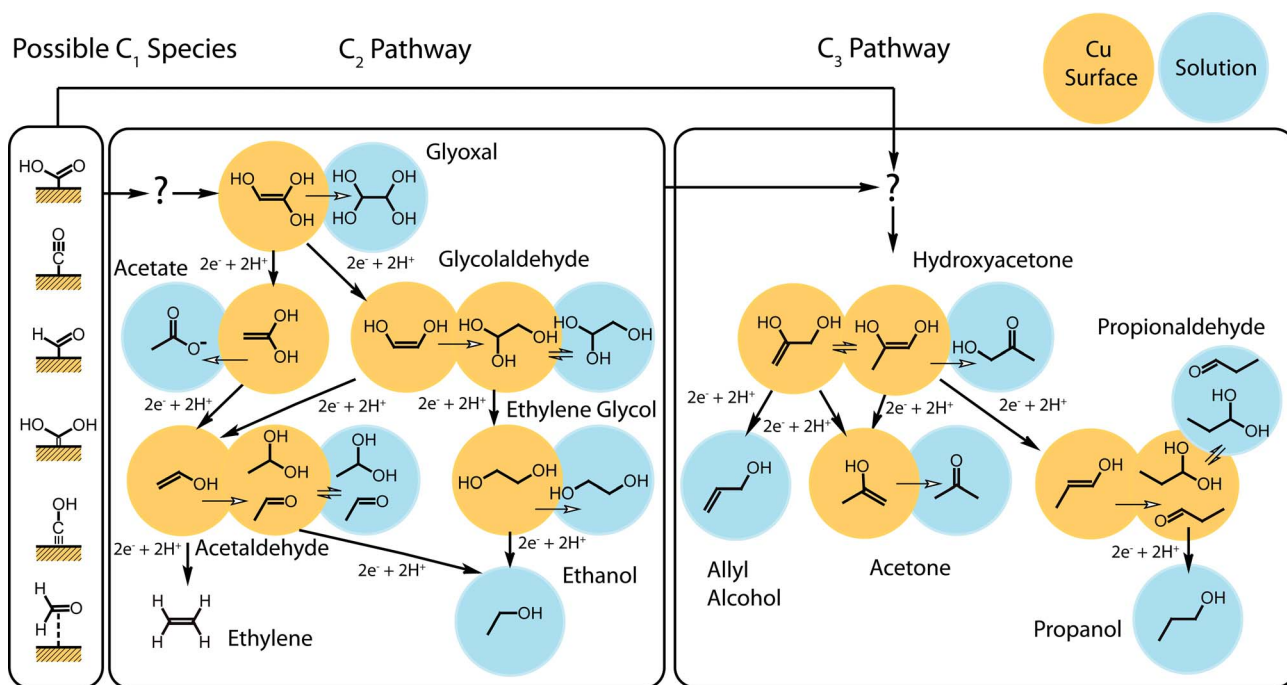


Fig. 7 Proposed reaction pathway for C_2 and C_3 products with enol-like surface intermediates. Arrows between overlapping circles indicate changes between the enol, keto, and diol form of each product. Arrows between non-overlapping circles indicate electrochemical reduction steps involving the addition of 2H^+ and 2e^- . For simplification, product names are intended to refer to all forms of the product.

which C_1 or C_2 species is involved in the C–C coupling step, the successive dehydroxylation of enol-like surface species is a reaction step that is repeated over and over and can explain the production of such a wide variety of C_2 and C_3 species.

In our scheme, after C–C bond formation the enol-like surface species quickly loses hydroxyls to form ethylene while desorption of intermediates along the way leads to the other observed products. We hypothesize that the enol-like surface species is kinetically accessible, but not the most thermodynamically stable, so once an intermediate has desorbed, it does not return to the ethylene pathway because it will not re-adsorb in the enol-like configuration. Thus, we expect that the addition of the products observed in this study to the electrolyte would not allow access to the ethylene pathway.

We suggest that enol-like surface species may be key intermediates on the pathway to multicarbon CO_2 reduction products. A crucial question remains as to which C_1 and C_2 surface intermediates are involved in C–C coupling reactions to form C_2 and C_3 products. Much of the uncertainty comes from not knowing which of the C_2 surface species is first to form on the pathway (whether glyoxal forms first or is preceded by another intermediate species that is not detected); likewise the initial C_3 species is unknown. Fig. 7 lists possible C_1 species present on the electrode based on intermediates from computational studies of CO_2 reduction to methane¹⁸ and methanol synthesis on a Cu(111) surface⁴³ as well as intermediates indicated by *in situ* Raman spectroscopy during CO_2 reduction.⁴⁴ Certainly, further experimental work is needed to fully elucidate CO_2 reduction mechanisms on copper. We expect that the results presented here regarding proposed C_2 and C_3 pathways can help guide the search for the C_1 and/or C_2 intermediates involved in C–C coupling.

Conclusions

New insight has been provided on the electrochemical reduction of CO_2 into fuels and chemicals on a Cu electrode surface. We employed a new experimental methodology involving a custom-designed electrolysis cell that allowed for increased concentration of reaction products in the liquid phase that enabled excellent sensitivity for identifying and quantifying reaction products by NMR. A total of 16 CO_2 reduction products are reported, significantly more than have ever been reported in any previous study on copper. Five of those 16 products are reported here for the very first time.

The products with the largest current efficiencies are the hydrocarbons methane and ethylene, while the remaining 14 products are oxygenates, 11 of which are C_2 and C_3 products. A number of these products are industrial chemicals with global-scale demand on the order of billions of kg/yr. Understanding selectivity for the CO_2 reduction reaction is of paramount importance; to do so, we studied trends in both the current efficiency and the partial current density (proportional to TOF) of each product over a range of potentials.

By analyzing trends in TOF for the multitude of reaction products, we deduced important mechanistic information. As previously observed, methane and ethylene are the dominant products of reaction. Their differing electrochemical behavior over the potential range, however, suggests that they have different rate determining steps. Conversely, the 12 multicarbon products show similarities in their potential-dependent behavior, a key clue in understanding the kinetics of C–C coupling. These 12 multicarbon products include a wide variety of oxygenates, *e.g.* alcohols, aldehydes, ketones, and carboxylic acids; any proposed pathway must account for similarities in their

potential-dependent behavior despite their differences in chemical functionality. To this end, we suggest two critical factors that can influence the reaction rate and selectivity for C_{2+} products: (1) coverage effects whereby the coverage and chemical identities of C_1 and C_2 surface species play major roles in determining which C_{2+} products are formed, and (2) the possibility of reaction intermediates proceeding through enol-like species on the electrode surface, a pathway involving a series of dehydroxylation steps that can account for the wide range of C_{2+} oxygenates as well as their simultaneous rise and subsequent fall in TOF, peaking at -1.05 V vs. RHE.

Many unanswered questions still remain as to the specifics of how the electrochemical reduction of CO_2 proceeds on a Cu surface. The results of this study, however, provide deeper insight into the reaction chemistry by (1) identifying and quantifying a number of new reaction products previously unreported to form a more complete picture of the reaction chemistry, and (2) using that new information to deduce reaction pathways. With more complete knowledge of the reaction chemistry, one can aspire to design catalysts capable of making desired products selectively and efficiently. The technology to electrochemically convert CO_2 to fuel and industrial chemicals would be a significant step toward a more sustainable future.

Acknowledgements

This work was supported by the Global Climate & Energy Project (GCEP) at Stanford University. TFJ gratefully acknowledges partial support provided by the MDV Innovator Award program at Mohr Davidow Ventures. KPK and ERC acknowledge support by the National Science Foundation Graduate Research Fellowship under Grant No. (DGE-1147470). ERC acknowledges support from the Ford Foundation. DNA acknowledges support from a Stanford Graduate Fellowship. The authors would also like to thank Zhebo Chen, Dr Arnold Forman, Dr Andrew A. Peterson, and Prof. Jens K. Nørskov for helpful discussions. Thanks to Dr Corey Liu of the Stanford Magnetic Resonance Laboratory for assistance on the 800 MHz NMR experiments and Dr Stephen R. Lynch of the Stanford Chemistry department NMR facility for help with the 600 MHz and 500 MHz experiments.

References

- N. S. Lewis and D. G. Nocera, *Proc. Natl. Acad. Sci. U. S. A.*, 2006, **103**, 15729–15735.
- M. Gattrell, N. Gupta and A. Co, *Energy Convers. Manage.*, 2007, **48**, 1255–1265.
- G. A. Olah, A. Goepfert and G. K. S. Prakash, *J. Org. Chem.*, 2009, **74**, 487–498.
- Y. Hori, in *Handbook of Fuel Cells: Fundamentals, Technology and Application*, ed. A. L. Wolf Vielstich, Hubert A. Gasteiger, VHC-Wiley, Chichester, 2003, vol. 2, pp. 720–733.
- T. W. Woolerton, S. Sheard, E. Pierce, S. W. Ragsdale and F. A. Armstrong, *Energy Environ. Sci.*, 2011, **4**, 2393–2399.
- A. Bandi, *J. Electrochem. Soc.*, 1990, **137**, 2157–2160.
- M. Azuma, K. Hashimoto, M. Hiramoto, M. Watanabe and T. Sakata, *J. Electrochem. Soc.*, 1990, **137**, 1772–1778.
- T. Yamamoto, D. A. Tryk, K. Hashimoto, A. Fujishima and M. Okawa, *J. Electrochem. Soc.*, 2000, **147**, 3393–3400.
- R. D. L. Smith and P. G. Pickup, *Electrochem. Commun.*, 2010, **12**, 1749–1751.
- S. Ikeda, T. Takagi and K. Ito, *Bull. Chem. Soc. Jpn.*, 1987, **60**, 2517–2522.
- E. B. Cole, P. S. Lakkaraju, D. M. Rampulla, A. J. Morris, E. Abelev and A. B. Bocarsly, *J. Am. Chem. Soc.*, 2010, **132**, 11539–11551.
- B. A. Rosen, A. Salehi-Khojin, M. R. Thorson, W. Zhu, D. T. Whipple, P. J. A. Kenis and R. I. Masel, *Science*, 2011, **334**, 643–644.
- Y. Hori, K. Kikuchi and S. Suzuki, *Chem. Lett.*, 1985, 1695–1698.
- M. Gattrell, N. Gupta and A. Co, *J. Electroanal. Chem.*, 2006, **594**, 1–19.
- D. T. Whipple and P. J. A. Kenis, *J. Phys. Chem. Lett.*, 2010, **1**, 3451–3458.
- Y. Hori, A. Murata and R. Takahashi, *J. Chem. Soc., Faraday Trans. 1*, 1989, **85**, 2309–2326.
- Y. Hori, R. Takahashi, Y. Yoshinami and A. Murata, *J. Phys. Chem. B*, 1997, **101**, 7075–7081.
- A. A. Peterson, F. Abild-Pedersen, F. Studt, J. Rossmeisl and J. K. Nørskov, *Energy Environ. Sci.*, 2010, **3**, 1311–1315.
- W. J. Durand, A. A. Peterson, F. Studt, F. Abild-Pedersen and J. K. Nørskov, *Surf. Sci.*, 2011, **605**, 1354–1359.
- K. J. P. Schouten, Y. Kwon, C. J. M. van der Ham, Z. Qin and M. T. M. Koper, *Chem. Sci.*, 2011, **2**, 1902–1909.
- Y. Hori, H. Konishi, T. Futamura, A. Murata, O. Koga, H. Sakurai and K. Oguma, *Electrochim. Acta*, 2005, **50**, 5354–5369.
- R. Vidal and A. C. West, *J. Electrochem. Soc.*, 1995, **142**, 2682–2689.
- J. Ghijsen, L. H. Tjeng, J. Vanelp, H. Eskes, J. Westerink, G. A. Sawatzky and M. T. Czyzyk, *Phys. Rev. B*, 1988, **38**, 11322–11330.
- NIST X-ray Photoelectron Spectroscopy Database, Version 4.0 (National Institute of Standards and Technology, Gaithersburg, 2008); <http://srdata.nist.gov/xps2>.
- D. van der Vliet, D. S. Strmcnik, C. Wang, V. R. Stamenkovic, N. M. Markovic and M. T. M. Koper, *J. Electroanal. Chem.*, 2010, **647**, 29–34.
- H. Shibata, J. A. Moulijn and G. Mul, *Catal. Lett.*, 2008, **123**, 186–192.
- D. M. Oxtoby, W. A. Freeman and T. F. Block, *Chemistry Science of Change*, Brooks/Cole, Belmont, CA, 2003.
- CRC Handbook of Chemistry and Physics*, 91st Edition (Internet Version 2011), CRC Press/Taylor and Francis, Boca Raton, FL, 2011.
- Y. Hori, I. Takahashi, O. Koga and N. Hoshi, *J. Phys. Chem. B*, 2002, **106**, 15–17.
- M. Le, M. Ren, Z. Zhang, P. T. Sprunger, R. L. Kurtz and J. C. Flake, *J. Electrochem. Soc.*, 2011, **158**, E45–E49.
- A. A. Peterson, F. Abild-Pedersen, F. Studt, J. Rossmeisl and J. K. Nørskov, *Energy Environ. Sci.*, 2010, **3**, 1311–1315.
- K. W. Loeffler, C. A. Koehler, N. M. Paul and D. O. De Haan, *Environ. Sci. Technol.*, 2006, **40**, 6318–6323.
- L. C. Gruen and P. T. McTigue, *J. Chem. Soc.*, 1963, 5217.
- G. C. S. Collins and W. O. George, *J. Chem. Soc. B*, 1971, 1352.
- Z. Rappoport, ed., *The Chemistry of Enols*, 1990.
- R. P. Bell, M. H. Rand and K. M. A. Wynne-Jones, *Trans. Faraday Soc.*, 1956, **52**, 1093–1102.
- Y. Kwon, S. C. S. Lai, P. Rodriguez and M. T. M. Koper, *J. Am. Chem. Soc.*, 2011, **133**, 6914–6917.
- L. D. Burke and J. A. Collins, *J. Appl. Electrochem.*, 1999, **29**, 1427–1438.
- H. Noda, S. Ikeda, Y. Oda and K. Ito, *Chem. Lett.*, 1989, 289–292.
- S. A. Vilekar, I. Fishtik and R. Datta, *J. Electrochem. Soc.*, 2010, **157**, B1040–B1050.
- N. Krstajic, M. Popovic, B. Grgur, M. Vojnovic and D. Sepa, *J. Electroanal. Chem.*, 2001, **512**, 16–26.
- W. Tang, A. A. Peterson, A. S. Varela, Z. P. Jovanov, L. Bech, W. J. Durand, S. Dahl, J. K. Nørskov and I. Chorkendorff, *Phys. Chem. Chem. Phys.*, 2012, **14**, 76–81.
- Y. F. Zhao, Y. Yang, C. Mims, C. H. F. Peden, J. Li and D. H. Mei, *J. Catal.*, 2011, **281**, 199–211.
- R. Kostecki and J. Augustynski, *Ber. Bunsenges. Phys. Chem.*, 1994, **98**, 1510–1515.